Modeling of Biomimetic Robotic Fish Propelled by An Ionic Polymer–Metal Composite Caudal Fin

Zheng Chen, *Student Member, IEEE*, Stephan Shatara, and Xiaobo Tan, *Member, IEEE*

Abstract—In this paper, a physics-based model is proposed for a biomimetic robotic fish propelled by an ionic polymer–metal composite (IPMC) actuator. Inspired by the biological fin structure, a passive plastic fin is further attached to the IPMC beam. The model incorporates both IPMC actuation dynamics and the hydrodynamics, and predicts the steady-state cruising speed of the robot under a given periodic actuation voltage. The interactions between the plastic fin and the IPMC actuator are also captured in the model. Experimental results have shown that the proposed model is able to predict the motion of robotic fish for different tail dimensions. Since most of the model parameters are expressed in terms of fundamental physical properties and geometric dimensions, the model is expected to be instrumental in optimal design of the robotic fish.

Index Terms—Biologically inspired robots, hydrodynamic modeling, ionic polymer–metal composites, robotic fish.

I. INTRODUCTION

AQUATIC animals (e.g., fishes, cetaceans, etc.) are ultimate examples of superior swimmers as a result of millions of years of evolution, endowed with a variety of morphological and structural features for moving through water with speed, agility, and efficiency [1], [2]. Intrigued by the remarkable feats in biological swimming and driven by the desire to mimic such capabilities, extensive theoretical [3], [4], experimental [5], [6], and computational [7] research has been conducted to understand hydrodynamic propulsion and maneuvering.

Recent years have also witnessed significant effort in the development of aquatic robots or robotic fish [8]–[15]. Motivated by fish fins, a number of researchers have studied the use of oscillating foils as propulsion devices for underwater vehicles or robots [13], [16]–[18]. While the existing work has been predominantly focused on rigid, oscillating plates or foils driven by motors [13], [16], [17], robotic fish using emerging soft actuation materials are gaining increasing interest. Electroactive polymers (EAPs), also known as artificial muscles, are attractive for aquatic robots because they are flexible and produce significant bending deformations under low voltages (several volts) [19], [20]. Two particularly promising classes of EAP materials are ionic polymer–metal composites (IPMCs) [19], [21] and conjugated polymers [20], [22]–[24]. IPMC-based robotic fish have been reported by several groups [9], [11], [12], [25]–[27]. An IPMC sample typically consists of a thin ion-exchange membrane (e.g., Nafion), chemically plated on both surfaces with a noble metal as electrode [28]. When a voltage is applied across an IPMC, transport of hydrated cations and water molecules within the membrane, and the associated electrostatic interactions lead to bending motions, and hence the actuation effect.

A faithful model is desirable for both optimal design [29] and control [30] of an underwater robot. For instance, Boyer *et al.* presented a dynamic model for 3-D eel-like robot [31]. Morgansen *et al.* investigated geometric methods for modeling and control of free-swimming and rigid fin-actuated underwater vehicles [13]. There have been limited studies related to modeling of flexible fins. A finite-element method was adopted by Yim *et al.* to model the motion of an IPMC actuator underwater [32], where an empirical *RC* circuit was used to predict the bending moment of IPMC under actuation. The added-mass effect due to acceleration of surrounding water was ignored in modeling hydrodynamic interactions, and the authors presented only simulation results. Modeling of IPMC actuators in underwater operations was also studied by Brunetto *et al.* [33]. However, there actuation dynamics of IPMC was represented by a frequency-dependent coupling term, which was essentially the empirical frequency response and did not capture the fundamental physics of IPMC. Furthermore, the experimental results in [33] were limited to a clamped IPMC beam in water, and no attempt was made to validate the model on a free-swimming robot. Recently, Porfiri and coworkers investigated the hydrodynamics of an IPMC beam using numerical computation [34] and digital particle image velocimetry (DPIV) measurements [35]. Although their work was very interesting, it was limited to a clamped IPMC beam only and the actuation dynamics of IPMC was not considered.

In this paper, we present, to our best knowledge, the *first* model for IPMC-propelled robotic fish that captures the intrinsic actuation physics of IPMC, and the complex hydrodynamic interactions between IPMC and fluid, and is validated in experiments on a free-swimming robotic fish prototype. Inspired by biological fish fins, where passive, collagenous membranes are driven by muscle-controlled fin rays [1], we have attached a passive, plastic fin to the tip of IPMC to enhance propulsion. In this paper, we call such a fin structure as *hybrid tail*. The proposed model incorporates the interactions of the passive fin with both the IPMC actuator and the fluid, allowing us to simultaneously capture the passive fin's role in boosting propulsion and its loading effect on the IPMC beam. The model is used

to predict the cruising speed of robotic fish, given a periodic actuation voltage to the IPMC fin. A more detailed account of the approach follows.

Based on the elongated-body propulsion theory of Lighthill [36], [37], the steady-state velocity of a swimming fish is related to the bending displacement and the slope of the tail end. The key of the modeling work is then to derive the motion of the hybrid tail under IPMC actuation and hydrodynamic interactions. Modeling of the hybrid tail starts with a fourth-order partial differential equation (PDE) that can capture the beam dynamics of IPMC in fluid. It incorporates the hydrodynamic force acting on the IPMC beam and the driving force introduced by actuation of IPMC. A mode-summation method is employed to obtain the solution to the PDE. The distributed bending moment generated by an actuation input is obtained using a physical, yet compact, model that captures the internal ion dynamics of IPMC [38]. In order to evaluate the actuation-induced generalized forces for the mode equations, we decompose the distributed moment into a distributed force along the length and a concentrated bending moment at the beam end, which would generate the same bending moment along the length. The model is then extended to capture the interactions between the IPMC and the passive fin. The hydrodynamic force acting on the passive fin is replaced by a concentrated moment and the force acting at the tip of IPMC actuator, which can be incorporated into the beam dynamics to obtain an analytical expression for the motion of hybrid tail.

Experiments have been performed to identify model parameters and validate the model. It is found that the model can predict well the cruising speed of the robot at different operating frequencies, for different tail dimensions. Since most of the parameters in the proposed model are expressed in terms of fundamental physical properties and geometric dimensions, the model will be instrumental for optimal design of the IPMC-propelled robotic fish to achieve good speed and efficiency.

The remainder of the paper is organized as follows. A prototype of robotic fish is described in Section II. The proposed model is presented in Section III. Experimental results on model validation are presented in Section IV. Finally, concluding remarks are provided in Section V.

II. DESCRIPTION OF IPMC-PROPELLED ROBOTIC FISH

Fig. 1(a) shows the schematic of the robotic fish, and Fig. 1(b) shows a prototype, which is an upgraded version of the one reported in [12]. The fish is designed to be fully autonomous and serve as a mobile, aquatic sensing platform. It consists of a rigid body and an IPMC caudal fin. Two gold-coated copper electrodes are used for IPMC to reduce corrosion of the electrodes in water. Corrosion of the electrodes results in high resistance of the contact, which would reduce the actuation performance of the IPMC tail and consume more electrical power. The IPMC actuator is further covered by a passive plastic fin to enhance propulsion. The rigid shell of the fish was custom-made to reduce the wetted surface, while having enough interior room to house rechargeable batteries and various electronic components for control, sensing, wireless communication, and navigation.
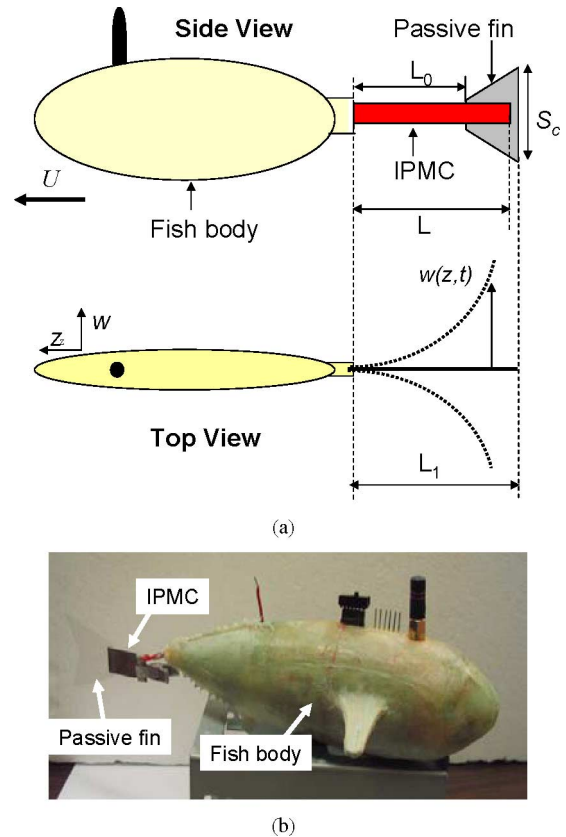

Fig. 1. (a) Schematic of the robotic fish. (b) Prototype of the robotic fish.

All of these components are contained in a water-proof packaging with necessary wires and pins exposed for charging batteries and driving IPMC actuator. Without the tail, the fish is about 20 cm in length and 5.7 cm in diameter. Total volume is about 180 cm^3. The fish body is in a water drop shape, which is expected to lead to good hydrodynamic efficiency. The Reynolds number of the swimming robotic fish is given by UD_0/ν, where U is the speed of the robot, D_0 is the body diameter, and $\nu = 10^{-6} \text{ m}^2/\text{s}$ is the kinematic viscosity of water. With a speed U of about 0.02 m/s (see Section IV-C), the Reynolds number of the robot is of the order of 1000. The total weight of the robotic fish is about 290 g. The shape and configuration of the robot put it into the category of carangiform fish.

III. MODEL

In this section, we first review Lighthill's theory on elongated-body propulsion (see Section III-A). IPMC beam dynamics in fluid is discussed next, considering general force and moment inputs (see Section III-B). This is followed by detailed consideration of actuation-induced bending moment in the model, as well as the load contribution to the IPMC beam from the passive fin (see Section III-C). Finally, the model for computing the speed of IPMC-propelled robotic fish is obtained by merging Lighthill's theory and the hybrid tail dynamics (see Section III-D).

A. Lighthill's Theory of Elongated-Body Propulsion

A body is considered elongated if its cross-sectional area changes slowly along its length. The robotic fish described in Section II is thus elongated and Lighthill's theory [37] applies.

Suppose that the tail is bending periodically with the bending displacement at z denoted by $w(z,t)$. See Fig. 1(a) for notation. At the steady state, the fish will achieve a periodic, forward motion with some mean speed U. In the discussion here, the word "mean" refers to the average over one period. The mean thrust $\overline{T}$ produced by the tail can be calculated as

$$\overline{T} = \left[\frac{m}{2} \left(\overline{\left(\frac{\partial w(z,t)}{\partial t} \right)^2} - U^2 \overline{\left(\frac{\partial w(z,t)}{\partial z} \right)^2} \right) \right]_{z=L_1} \quad (1)$$

where $z = L_1$ denotes the end of tail, $\overline{(\cdot)}$ denotes the *mean* value, and m is the virtual mass density at $z = L_1$, expressed as

$$m = \frac{1}{4}\pi S_c^2 \rho_w \beta \quad (2)$$

where S_c is the width of the tail at the end $z = L_1$, ρ_w is the fluid density, and β is a nondimensional parameter close to 1. Equation (1) indicates that the mean thrust depends only on the lateral velocity ($\partial w/\partial t$) and the slope ($\partial w/\partial z$) at the tail end. A cruising fish, under inviscid flow conditions, will experience a drag force F_D as

$$F_D = \frac{C_D \rho_w U^2 S}{2} \quad (3)$$

where S is the wetted surface area and C_D is the drag coefficient. At the steady state, the mean thrust $\overline{T}$ is balanced by the drag F_D, from which one can solve the cruising speed U as

$$U = \left[\sqrt{ \frac{m \overline{(\partial w(z,t)/\partial t)^2}}{C_D \rho_w S + m \overline{(\partial w(z,t)/\partial z)^2}} } \right]_{z=L_1}. \quad (4)$$

Since the speed of the fish is related to the lateral velocity and the slope of the trailing edge, one needs to fully understand the actuation dynamics of the tail.

B. IPMC Beam Dynamics in Fluid

In order to obtain the full actuation model of IPMC, we start with a fourth-order PDE for the dynamic deflection function $w(z,t)$ [39] as

$$YI\frac{\partial^4 w(z,t)}{\partial z^4} + C\frac{\partial w(z,t)}{\partial t} + \rho_m A\frac{\partial^2 w(z,t)}{\partial t^2} = f(z,t) \quad (5)$$

where Y, I, C, ρ_m, and A denote the effective Young's modulus, the area moment of inertia, the internal damping ratio, the density, and the cross-sectional area of the IPMC beam, respectively, and $f(z,t)$ is the distributed force density acting on the beam.

Converting (5) into the Laplace domain, we obtain

$$YI\frac{\partial^4 w(z,s)}{\partial z^4} + Csw(z,s) + \rho_m As^2 w(z,s) = F(z,s). \quad (6)$$

The force on the beam consists of two components, the hydrodynamic force F_{hydro} from water and the driving force F_{drive} due to the actuation of IPMC

$$F(z,s) = F_{\text{hydro}}(z,s) + F_{\text{drive}}(z,s). \quad (7)$$

The hydrodynamic force acting on the IPMC beam can be expressed as [40]

$$F_{\text{hydro}}(z,s) = -\rho_w \frac{\pi}{4} W^2 s^2 \Gamma_1(\omega) w(z,s), \qquad 0 \leq z \leq L \quad (8)$$

where W is the width of the IPMC beam, $\Gamma_1(\omega)$ is the hydrodynamic function for the IPMC beam subject to an oscillation with radial frequency ω, and ρ_w is the density of fluid. The hydrodynamic function for a rectangular beam can be represented as [40]

$$\Gamma_1(\omega) = \Omega(R_e)\left[1 + \frac{4iK_1\left(-i\sqrt{iR_e}\right)}{\sqrt{iR_e}K_0\left(-i\sqrt{iR_e}\right)}\right] \quad (9)$$

where the Reynolds number R_e of a vibrated beam in water is given by

$$R_e = \frac{\rho_w W^2 \omega}{4\eta}$$

K_0 and K_1 are modified Bessel functions of the third type, $\Omega(R_e)$ is the correction function associated with the rectangular beam cross section [40], and η is the viscosity of fluid.

With (7) and (8), the beam dynamics equation (6) can be written as

$$YI\frac{\partial^4 w(z,s)}{\partial z^4} + Csw(z,s) + (\mu_m + m_d\Gamma_1)s^2 w(z,s) = F_{\text{drive}}(z,s) \quad (10)$$

where $m_d = \rho_w(\pi/4)W^2$ is the added mass and $\mu_m = \rho_m A$ is the mass of IPMC per unit length. Under harmonic oscillation with frequency ω, we can denote

$$\mu_v = \mu_m + m_d\text{Re}(\Gamma_1) \quad (11)$$

$$C_v = C - m_d\omega\text{Im}(\Gamma_1) \quad (12)$$

where μ_v is the equivalent mass of IPMC per unit length in water and C_v is the equivalent damping coefficient of IPMC in water. $\text{Re}(\cdot)$ and $\text{Im}(\cdot)$ are the functions that get the real part and the imaginary part from a complex value, respectively. Equation (12) means that the damping of IPMC vibration in water includes both the internal damping in IPMC and the frequency-dependent external damping caused by fluid. With (11) and (12), (10) can be written as [33]

$$YI\frac{\partial^4 w(z,s)}{\partial z^4} + C_v sw(z,s) + \mu_v s^2 w(z,s) = F_{\text{drive}}(z,s). \quad (13)$$

According to the mode analysis method, we can express the solution to (13) as the sum of different modes [41] as

$$w(z,s) = \sum_{i=1}^{\infty} \varphi_i(z) q_i(s) \quad (14)$$

where $\phi_i(z)$ is the beam shape for the ith mode and $q_i(s)$ is the corresponding generalized coordinate. The mode shape $\phi_i(z)$

takes the form

$$\varphi_i(z) = \cosh(\lambda_i z) - \cos(\lambda_i z) - \beta_i(\sinh(\lambda_i z) - \sin(\lambda_i z)) \tag{15}$$

where λ_i can be obtained by solving

$$1 + \cos(\lambda_i L)\cosh(\lambda_i L) = 0$$

and

$$\beta_i = \frac{\sinh(\lambda_i L) - \sin(\lambda_i L)}{\cosh(\lambda_i L) + \cos(\lambda_i L)}.$$

The generalized coordinate $q_i(s)$ can be represented as

$$q_i(s) = f_i(s)Q_i(s) \tag{16}$$

where $f_i(s)$ is the generalized force

$$Q_i(s) = \frac{1}{s^2 + 2\xi_i\omega_i s + \omega_i^2} \tag{17}$$

and the natural frequency ω_i and the damping ratio ξ_i for the ith mode are

$$\omega_i = \frac{C_i^2}{L^2}\sqrt{\frac{YI}{\mu_v(\omega_i)}} \tag{18}$$

$$\xi_i = \frac{C_v(\omega_i)}{2\mu_v(\omega_i)\omega_i} \tag{19}$$

and $C_i = \lambda_i L$. Noting that $\Gamma_1(\omega)$ is almost a constant value in the frequency region around ω_i, one can consider $\mu_v(\omega_i)$ as a constant in (18). Therefore, ω_i can be obtained approximately. Then, with ω_i, ξ_i can be obtained from (19). The generalized force $f_i(s)$ is obtained from F_{drive} as

$$f_i(s) = \frac{1}{M_i}\int_0^L F_{\text{drive}}(z,s)\varphi_i(z)\,dz$$

where M_i is the generalized mass

$$M_i(s) = \int_0^L \mu_v\varphi_i^2(z)\,dz = \mu_v L. \tag{20}$$

The next step is to derive the generalized force $f_i(s)$ from the moment generated by IPMC actuation and from the hydrodynamic force acting on the passive fin but transmitted to the IPMC beam.

C. Actuation Model of the Tail

In our earlier work [38], we fully investigated the electrical dynamics of IPMC to obtain the moment generated within IPMC, but there, the beam dynamics in water was not considered. In the following, we will incorporate both electrical dynamics and hydrodynamic interactions into a full-actuation model for IPMC hybrid tail in water.

The ion movement inside an IPMC, under the influence of an applied electric field, leads to a distribution of net charge density along the thickness direction of IPMC. A physics-based model for IPMC proposed by Nemat-Nasser and Li [42] relates the actuation-induced (axial) stress proportionally to the charge density, through electromechanical coupling. Variation of the actuation-induced stress along the thickness direction,

thus, results in a bending moment at each point along the length direction. Our work on physics-based, control-oriented modeling of IPMC actuators [38] further incorporates the effect of distributed surface resistance. The latter leads to nonuniform potential difference along the length direction, which, in turn, leads to actuation-induced bending moment that varies along the length direction, referred to as distributed bending moment in this paper. See [38] for further details.

With distributed surface resistance, we can relate the actuation-induced bending moment $M_{\text{IPMC}}(z,s)$ at point z to the actuation voltage $V(s)$ by an infinite-dimensional transfer function [38] as

$$\begin{aligned} & M_{\text{IPMC}}(z,s) \\ & = \frac{\alpha_0 WKk_e(\gamma(s) - \tanh(\gamma(s)))}{(s\gamma(s) + K\tanh(\gamma(s)))} \\ & \times \frac{\cosh(\sqrt{B(s)}z) - \sinh(\sqrt{B(s)}z)\tanh(\sqrt{B(s)}L)}{1 + r_2\theta(s)}V(s) \end{aligned} \tag{21}$$

with

$$\theta(s) \triangleq \frac{Wk_e s\gamma(s)(s+K)}{h(s\gamma(s) + K)}$$

$$B(s) \triangleq \sqrt{r_1\left(\frac{\theta(s)}{(1 + r_2\theta(s))} + \frac{2}{R_p}\right)}$$

$$\gamma(s) \triangleq \sqrt{\frac{s+K}{d}}$$

$$K \triangleq \frac{F^2 dC^-}{\kappa_e RT}\left(1 - C^-\Delta V\right)$$

where α_0 is an electromechanical coupling constant, d is the ionic diffusivity, R is the gas constant, F is Faraday's constant, T is the absolute temperature, C^- is the anion concentration, ΔV is the volumetric change, x is the coordinate defined in the thickness direction, κ_e is the effective dielectric constant of the polymer, r_1 is the electrode resistance per unit length in the length direction, r_2 is the electrode resistance per unit length in the thickness direction, and R_p is the through-polymer resistance per unit length. W, L, and h are the width, length, and half thickness of the IPMC beam, respectively.

We replace the moment $M_{\text{IPMC}}(z,s)$ induced by actuation by three components: a distributed force density $F_d(z,s)$ acting along the length, a concentrated force $F_c(L,s)$, and a moment $M(L,s)$ acting at the IPMC tip $z = L$, where

$$F_c(L,s) = -\left.\frac{\partial M_{\text{IPMC}}(z,s)}{\partial z}\right|_{z=L}$$

$$F_d(z,s) = \frac{\partial^2 M_{\text{IPMC}}(z,s)}{\partial z^2} \tag{22}$$

$$M(L,s) = M_{\text{IPMC}}(L,s). \tag{23}$$

The rationale of this replacement is that these components can generate the same bending moment as $M_{\text{IPMC}}(z,s)$. See Appendix A for the details of this justification. With (21), it can
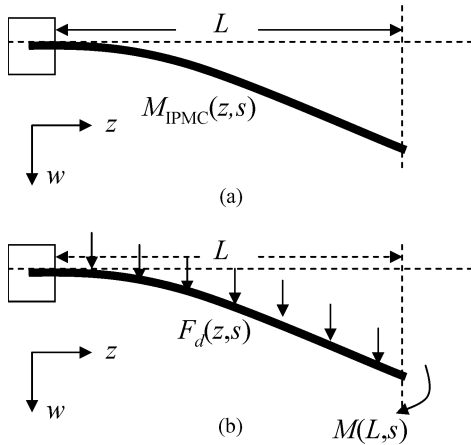
Fig. 2. Original moment in (a) is replaced by a distributed force density and a concentrated bending moment in (b).

be verified that $F_c(L, s) \equiv 0$. Then, the generalized force can be obtained as [41]

$$f_{1i}(s) = \frac{1}{M_i} \left(\int_0^L F_d(z, s) \varphi_i(z) \, dz + M(L, s) \varphi_i'(L) \right). \quad (24)$$

Fig. 2 shows that the original moment is replaced by a distributed force density and a concentrated moment. With the aforementioned replacement, we can derive the models for the IPMC tail-only case and the hybrid tail case.

1) With IPMC Tail Only: With (22) and (23), the generalized force (24) can be written as

$$f_{1i}(s) = H_{fi}(s) V(s) \quad (25)$$

where

$$H_{fi}(s)$$
$$= \frac{1}{2M_i} \begin{pmatrix} (a - b)(a_L + b_L - c_L - d_L) \\ -\beta_i(a - b)(a_L - b_L + jc_L - jd_L) \end{pmatrix}$$
$$+ \frac{\alpha_0 W K k_e (\gamma(s) - \tanh(\gamma(s)))}{M_i (s\gamma(s) + K \tanh(\gamma(s)))} \frac{\varphi_i'(L)}{(1 + r_2\theta(s)) \cosh(cL)} \quad (26)$$

and

$$a = \frac{\alpha_0 W K k_e (\gamma(s) - \tanh(\gamma(s)))}{(s\gamma(s) + K \tanh(\gamma(s)))} \frac{B(s)}{1 + r_2\theta(s)} \quad (27)$$

$$b = a \tanh(\sqrt{B(s)}L) \qquad c = \sqrt{B(s)} \quad (28)$$

$$a_L = \frac{\sinh((c + \lambda_i)L)}{c + \lambda_i} \qquad b_L = \frac{\sinh((c - \lambda_i)L)}{c - \lambda_i} \quad (29)$$

$$c_L = \frac{\sinh((c + j\lambda_i)L)}{c + j\lambda_i} \qquad d_L = \frac{\sinh((c - j\lambda_i)L)}{c - j\lambda_i}. \quad (30)$$

See Appendix B for the derivation of $H_{fi}(s)$.

From (14), one can then get the transfer function $H_1(L, s)$ relating $w(L, s)$ to $V(s)$ as

$$H_1(L, s) = \frac{w(L, s)}{V(s)} = \sum_{i=1}^\infty \varphi_i(L) H_{fi}(s) Q_i(s). \quad (31)$$
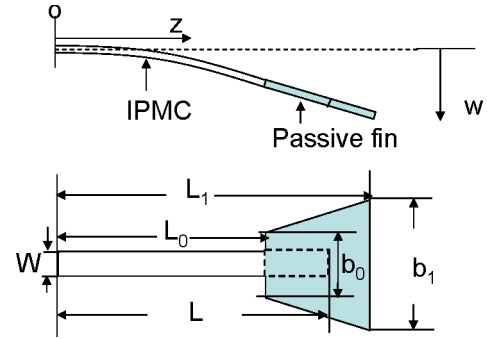

Fig. 3. Illustration of an IPMC beam with a passive fin. The lower schematic shows the definitions of dimensions.

We can also derive the transfer function $H_{1d}(L, s)$ relating the slope of the beam $\partial w(L, s)/\partial z$ to the input voltage $V(s)$ as

$$H_{1d}(L, s) = \frac{(\partial w(L, s)/\partial z)}{V(s)} = \sum_{i=1}^\infty \varphi_i'(L) H_{fi}(s) Q_i(s). \quad (32)$$

2) Hybrid Tail: From (1) and (2), the tail width S_c at the end has a significant impact on the speed U. One could increase S_c by simply using a wider IPMC beam. Due to the IPMC actuation mechanism, however, a too wide beam (i.e., plate) will produce curling instead of bending motion, and is thus not desirable. Therefore, it has been chosen to increase the edge width by attaching a passive plastic piece, as illustrated in Fig. 3. While such a hybrid tail is expected to increase the thrust, one has to also consider that the extra hydrodynamic force on the passive fin adds to the load of IPMC, and may reduce the bending amplitude. Therefore, it is necessary to model these interactions carefully.

The hydrodynamic force acting on the passive fin can be written as [40]

$$f_{\text{tail}}(z, s) = -\frac{\pi}{4} \rho_w s^2 b(z)^2 \Gamma_2(\omega) w(z, s), \qquad L_0 \le z \le L_1 \quad (33)$$

where $\Gamma_2(\omega)$ is the hydrodynamic function of the passive fin. Note that the hydrodynamic force acting on the active IPMC beam has been incorporated in (10), and therefore, only the hydrodynamic force on the passive fin needs to be considered here. Since the passive fin used is very light, its inertial mass is negligible compared to the propelled virtual fluid mass, and is thus ignored in the analysis here. Considering that the passive fin is rigid compared to IPMC, its width $b(z)$ and deflection $w(z, s)$ can be expressed as

$$b(z) = \frac{b_1 - b_0}{L_1 - L_0}(z - L_0) + b_0 \quad (34)$$

$$w(z, s) = w(L_0, s) + \frac{\partial w(L_0, s)}{\partial z}(z - L_0) \quad (35)$$

where b_0, b_1, L, L_0, and L_1 are as defined in Fig. 3. Then, one can calculate the moment introduced by the passive fin: for $L_0 \le z \le L_1$,
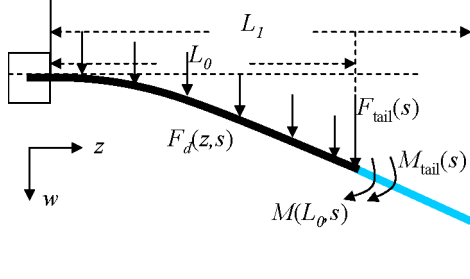
Fig. 4. Forces and moments acting on the hybrid tail.

$$M_{\text{fin}}(z,s) = \int_{L_0}^{L_1} f_{\text{tail}}(\tau,s)(\tau - z)\,d\tau$$

$$= \int_{L_0}^{L_1} f_{\text{tail}}(\tau,s)(\tau - L_0)\,d\tau$$

$$+ (L_0 - z)\int_{L_0}^{L_1} f_{\text{tail}}(\tau,s)\,d\tau. \quad (36)$$

If we define

$$M_{\text{tail}}(s) = \int_{L_0}^{L_1} f_{\text{tail}}(\tau,s)(\tau - L_0)\,d\tau,$$

$$F_{\text{tail}}(s) = \int_{L_0}^{L_1} f_{\text{tail}}(\tau,s)\,d\tau \quad (37)$$

then (36) can be written as

$$M_{\text{fin}}(z,s) = M_{\text{tail}}(s) + F_{\text{tail}}(s)(L_0 - z). \quad (38)$$

Fig. 4 shows the forces and moments acting on the hybrid tail.

One can obtain the generalized force as

$$f_{2i}(s) = \frac{1}{M_i}\left(\int_0^{L_0} F_d(z,s)\,\varphi_i(z)\,dz + \varphi_i(L_0)\,F_{\text{tail}}(s)\right)$$

$$+ \frac{(M_{\text{tail}}(s) + M(L_0,s))\varphi_i'(L_0)}{M_i} \quad (39)$$

where M_{tail} and F_{tail} are defined in (37), $F_d(z,s)$ and $M(L_0,s)$ are defined in (22) and (23).

Then, the transfer function relating $w(L_0,s)$ to $V(s)$ and that relating $w'(L_0,s) \triangleq \partial w(L_0,s)/\partial z$ to $V(s)$ can be found as

$$H_2(L_0,s) = \frac{(1 + F_s)A_s - B_s E_s}{(1 + C_s)(1 + F_s) - B_s J_s} \quad (40)$$

$$H_{2d}(L_0,s) = \frac{(1 + C_s)E_s - A_s J_s}{(1 + C_s)(1 + F_s) - B_s J_s} \quad (41)$$

where

$$A_s = H_1(L_0,s) \quad E_s = H_{1d}(L_0,s) \quad (42)$$

$$D = L_1 - L_0, \quad k = \frac{b_1 - b_0}{D}, \quad M_s = \frac{\pi}{4}s^2\Gamma_2(\omega)\rho_w$$

$$B_s = \sum_{i=1}^{\infty} \frac{\varphi_i(L_0)Q_i(s)}{M_i}M_s[\varphi_i'(L_0)k_a + \varphi_i(L_0)k_b] \quad (43)$$

$$C_s = \sum_{i=1}^{\infty} \frac{\varphi_i(L_0)Q_i(s)}{M_i}M_s[\varphi_i'(L_0)k_b + \varphi_i(L_0)k_c] \quad (44)$$

$$F_s = \sum_{i=1}^{\infty} \frac{\varphi_i'(L_0)Q_i(s)}{M_i}M_s[\varphi_i'(L_0)k_a + \varphi_i(L_0)k_b] \quad (45)$$

$$J_s = \sum_{i=1}^{\infty} \frac{\varphi_i'(L_0)Q_i(s)}{M_i}M_s[\varphi_i'(L_0)k_b + \varphi_i(L_0)k_c] \quad (46)$$

and

$$k_a = \frac{k^2 D^5}{5} + \frac{2kb_0 D^4}{4} + \frac{b_0^2 D^3}{3}$$

$$k_b = \frac{k^2 D^4}{4} + \frac{2kb_0 D^3}{3} + \frac{b_0^2 D^2}{2}$$

$$k_c = \frac{k^2 D^3}{3} + kb_0 D^2 + b_0^2 D. \quad (47)$$

See Appendix C for the detailed derivation. From (35), (40), and (41), one can obtain the transfer functions relating the bending displacement and the slope at $z = L_1$ to the voltage input $V(s)$ as follows:

$$H_3(L_1,s) \triangleq \frac{w(L_1,s)}{V(s)} = H_2(L_0,s) + H_{2d}(L_0,s)D$$

$$H_{3d}(L_1,s) \triangleq \frac{w'(L_0,s)}{V(s)} = H_{2d}(L_0,s). \quad (48)$$

D. Speed Model of Robotic Fish

Given a voltage input $V(t) = A_m\sin(\omega t)$ to the IPMC actuator, the bending displacement and the slope of the tail at the tip $z = L_1$ can be written as

$$w(L_1,t) = A_m|H(j\omega)|\sin(\omega t + \angle H(j\omega)) \quad (49)$$

$$\left.\frac{\partial w(z,t)}{\partial z}\right|_{z=L_1} = A_m|H_d(j\omega)|\sin(\omega t + \angle H_d(j\omega)) \quad (50)$$

where $\angle(\cdot)$ denotes the phase angle, and $H(s)$ and $H_d(s)$ represent $H_3(L_1,s)$ and $H_{3d}(L_1,s)$, respectively, obtained at the end of Section III-C. From (4), one can then obtain the steady-state speed U of the robotic fish under the actuation voltage $V(t) = A_m\sin(\omega t)$ as

$$U = \sqrt{\frac{mA_m^2\omega^2|H(j\omega)|^2}{2C_D\rho_w S + mA_m^2|H_d(j\omega)|^2}}. \quad (51)$$

One can easily extend (51) to periodic signals of other forms. For instance, the prototype in Fig. 1(b) uses square-wave voltage signals for ease of implementation. To derive the speed U, we can write out the Fourier series of a square wave. Then the velocity of the fish actuated under a square-wave voltage with amplitude A_m can be obtained as

$$U = \sqrt{\frac{m(8\omega^2 A_m^2/\pi^2)\sum_{n=1,3,5\cdots}^{\infty}|H(jn\omega)|^2}{C_D\rho_w S + m(8A_m^2/\pi^2)\sum_{n=1,3,5\cdots}^{\infty}((|H_d(jn\omega)|^2)/n^2)}}. \quad (52)$$

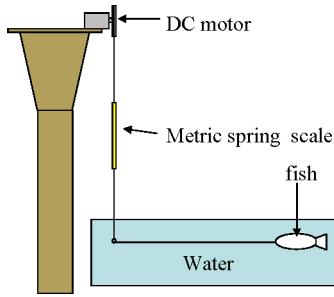Derivation of (52) is omitted here due to the space limitation.

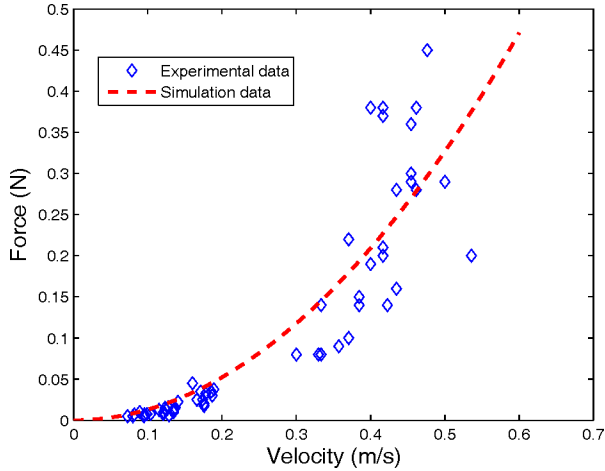Fig. 5.   Experimental setup for the drag force measurement.

Fig. 6.   Drag force versus velocity of the fish.

IV. EXPERIMENTAL VERIFICATION AND PARAMETERS IDENTIFICATION

In this section, three different types of experiments have been carried out for model identification and validation: 1) drag coefficient identification (see Section IV-A); 2) identification and validation of the actuation model for IPMC underwater with and without the passive fin (see Section IV-B); and finally, 3) validation of the model for fish motion with different tail dimensions (see Section IV-C).

A. Drag Coefficient Identification

The most important parameter related to the fish body is the drag coefficient C_D, which depends on the Reynolds number, the fitness ratio of the body, and the properties of the fish surface and fluid. In order to identify C_D, the fish was pulled with different velocities, and metric spring scales were used to measure the drag force F_D. With the measured drag force, velocity, and surface area of the fish, the drag coefficient C_D was calculated from (3). Fig. 5 illustrates the experimental setup for drag force measurement.

Through drag force measurement, one can get the plot of the drag force versus velocity. Based on (3), one can fit the experimental data with simulation data through the least-squares method to identify the drag coefficient. Fig. 6 shows the drag force versus the velocity of the fish. Table I shows the parameters related to the drag force.

TABLE I
PARAMETERS RELATED TO THE DRAG FORCE

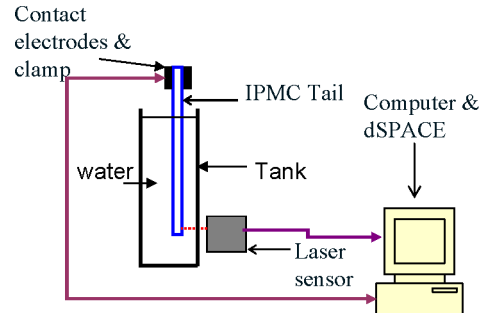| S	ρ_w	C_D
$218 \times 10^{-4} \mathrm{m}^2$	$1000 \mathrm{~kg/m}^3$	0.12

Fig. 7.   Experimental setup for identification and verification of IPMC actuation model in water.

B. Fish Tail Model Verification

To investigate the parameters related to the IPMC beam dynamics, the natural vibrations of IPMC in water and air were measured without actuation voltage applied to the IPMC. They were also used to verify $Q_1(s)$ for the first mode vibration. To investigate the hydrodynamic effect of passive fin on the IPMC beam, the frequency responses of the tail subject to voltage input were measured for both with and without the plastic fin. They were also used to verify the actuation models of IPMC. Fig. 7 shows the schematic of experimental setup. In the natural vibration testing, the tail was fixed in water and a mechanical impulse was applied at the tip to make the beam vibrate. The first-mode vibration was measured by a laser sensor (OADM 20I6441/S14F, Baumer Electric). In the frequency response testing, the fish tail was fixed in the water by a frame arm, and a sequence of sinusoid voltages with amplitude 3.3 V and frequency ranging from 0.05 to 10 Hz were applied to the IPMC. The lateral displacement of the IPMC beam was captured by a laser sensor, and the actuation voltage was measured by a dSPACE station (DS1104, dSPACE).

1) Beam Dynamics Identification: Since the actuation bandwidth of IPMC actuators is relatively low (up to a few hertz), it suffices to consider the first mode of the beam motion. The parameters related to the beam dynamics can be identified through passive vibration tests of IPMC in water. The first-mode vibration related to the step response of the second-order system $Q_1(s)$ [see (17)] is

$$y(t) = y(0) e^{-\xi_1 \omega_1 t} \cos\left(\omega_1 t \sqrt{1 - \xi_1^2}\right).$$

In the experiment, we tapped the tip of the cantilevered IPMC beam (submerged in water) and recorded the tip trajectory with the laser sensor as the beam underwent passive, damped oscillations. Fig. 8 shows both the simulation data and the experimental data on the tip displacement of the vibrating IPMC beam, where the beam dimensions were $L = 23$ mm and $W = 15$ mm.

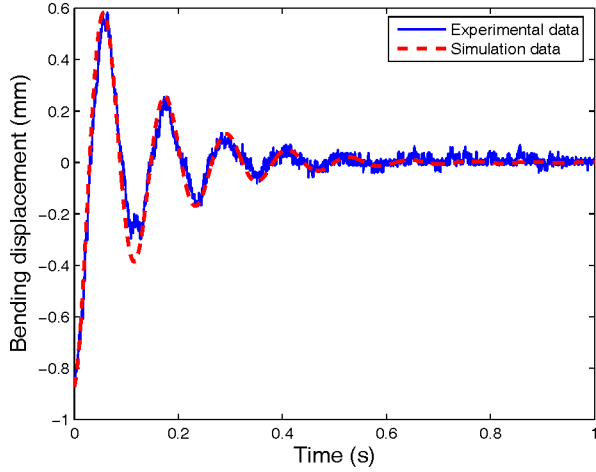Fig. 8. Passive, damped vibration of IPMC beam in water.

TABLE II
PARAMETERS IN IPMC BEAM DYNAMICS

C_v	μ_v	W	L
3.17	0.2 kg/m	15 mm	23 mm
h	C_1	Y	Γ_1
115 μm	1.8751	2.91 $\times 10^8$ Pa	1.07+0.04j

TABLE III
PARAMETERS RELATED TO THE ELECTRICAL DYNAMICS OF IPMC

F	T	R	C^-
96487 C/mol	300 K	8.3143 J/mol·K	1091 mol/m^3
r_1	r_2	d	κ_e
210 Ω/m	0.04 Ω·m	5.39 $\times 10^{-9}$m/s	2.48$\times 10^{-5}$ F/m
R_p	α_0		
38 Ω·m	0.08 J/C		

From Fig. 8, the natural frequency and damping ratio in water were identified to be $\omega_1 = 54$ rad/s, $\xi_1 = 0.14$. The hydrodynamic function of IPMC beam $\Gamma_1(\omega)$ can be simulated based on (9). The correction function $\Omega(\omega)$ for rectangular shape beam reported in [40] is used in the simulation. Around the natural frequency, one can pick $\mathrm{Re}(\Gamma_1) = 1.07$ and $\mathrm{Im}(\Gamma_1) = 0.04$. Based on (11), one can get μ_v. Based on (18) and (19), one can obtain Y and C_v. Table II shows all the parameters related to the beam dynamics.

2) Fish Tail Model Identification: In the fish tail model, some parameters can be directly measured, such as dimensions, temperature, resistance, and density of IPMC. Some parameters are physical constants, such as R, F, and ρ_w. Since $|C^-\Delta V| \ll 1$ [42], we take $1 - C^-\Delta V = 1$. Some parameters, such as k_e, α_0, and r_2 need to be identified through fitting the frequency responses with model simulation, which was discussed in [38]. Γ_2 can be identified through fitting the frequency response of hybrid tail with simulation data. Table III shows the parameters related to the electrical dynamics of IPMC. The dimensions of IPMC-only tail are shown in Table II. The dimensions of hybrid tail tail1 are shown in Table IV.

TABLE IV
DIMENSIONS OF FOUR TAILS (SEE FIG. 3 FOR THE DEFINITIONS OF DIMENSION VARIABLES)

	L_0(mm)	L(mm)	W(mm)	b_0(mm)	b_1(mm)	D(mm)
Tail 1	18	23	15	20	40	40
Tail 2	18	23	15	20	50	30
Tail 3	18	23	20	20	65	25
Tail 4	18	23	20	20	50	30
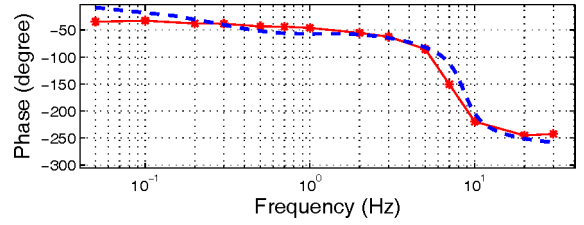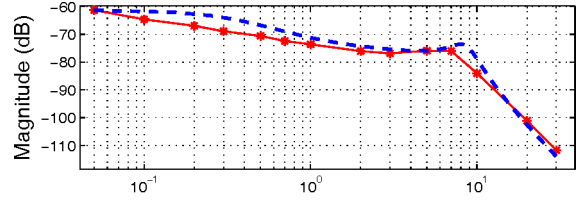
(a)
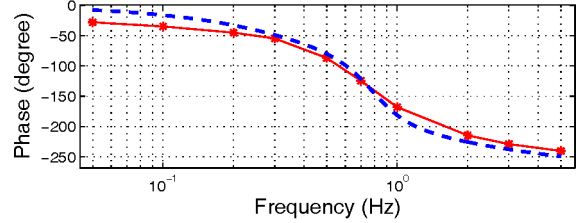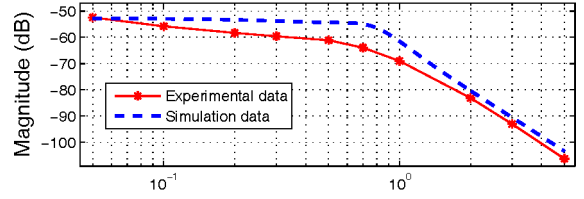
(b)

Fig. 9. Validation of model for IPMC operating underwater. Shown in the figure are the Bode plots for (a) model $H_1(L,s)$ without passive fin, and (b) model $H_3(L_1,s)$ with passive fin, in comparison with their experimental measurements.

The actuation model of IPMC with and without passive fin is verified. We applied sinusoidal voltage signals with amplitude 3.3 V and different frequencies to IPMC. Both the voltage input and the bending displacement output at the tail tip were measured to obtain the empirical frequency responses. In the case of an IPMC beam only, the displacement measurement was made at the beam tip; in the case of a hybrid tail, the displacement was measured at the tip of passive fin. In the simulation of the actuation models, only the first mode was taken into account, because the frequencies used were below or close to the first-mode resonant frequency. Fig. 9(a) compares the Bode plot of $H_1(L,s)$ (see (31) in Section III) with its empirical counterpart, and the agreement is good in both magnitude and phase. The cutoff
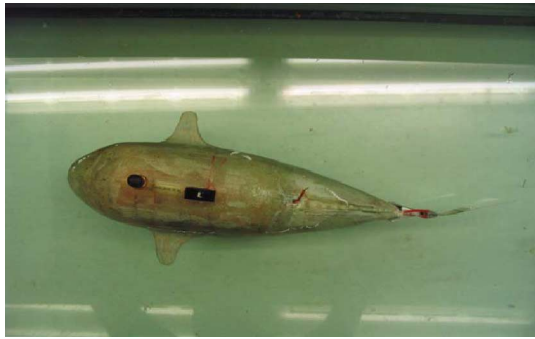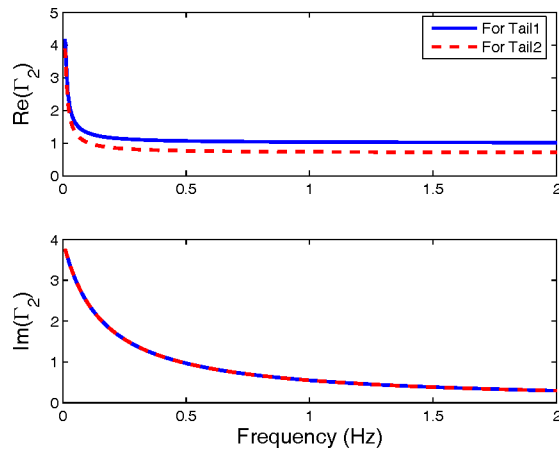
Fig. 10.   Snapshot of robotic fish in swimming test.

Fig. 11.   Identified Γ_2 for tail 1 and tail 2.

frequency is estimated to be about 8.6 Hz, which is consistent with the IPMC beam's natural frequency in water, as identified from the free-vibration experiment shown in Fig. 8. Fig. 9(b) compares the Bode plot of $H_3(L_1, s)$ (see (48) in Section III) and the measured frequency response from voltage input to the tail tip displacement for the hybrid tail. As can be seen in the figure, the cutoff frequency of the hybrid tail is much lower than that of an IPMC alone. This can be explained by the additional mass effect at the IPMC tip, introduced by the fluid pushed by the passive fin.

C. Speed Model Verification

To validate the speed model of the robotic fish, the velocities of the fish propelled by the IPMC under square-wave voltage inputs with amplitude 3.3 V and different frequencies were measured. In this experiment, the robotic fish swam freely in a tank marked with start and finish lines, and a timer recorded the time it took for the fish to travel the designated range after it reached the steady state. Fig. 10 shows a snapshot of the fish swimming in the tank.

The capability of the model in predicting cruising speed was verified for different operating frequencies, for different tail dimensions. The speed model for a square-wave input [see (52)] was applied to the robotic fish, as described in Section II. In the simulation of (52), we took the first three terms in each infinite series, which provided a good approximation to the sum
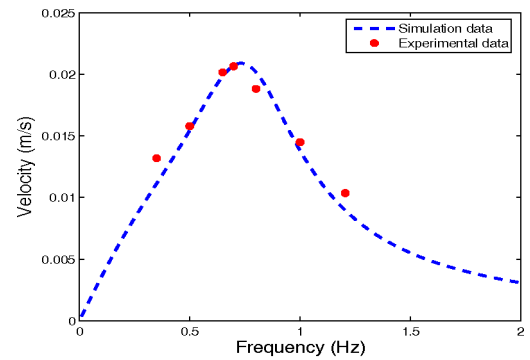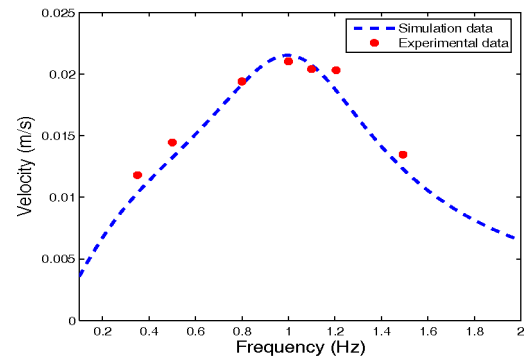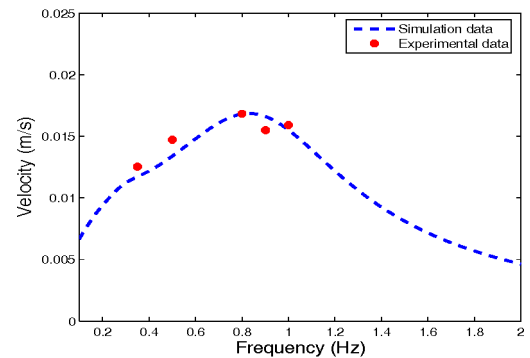
Fig. 12.   Verification of the motion model for the fish with different tails. (a) With tail 1. (b) With tail 2. (c) With tail 3. (d) With tail 4.

of infinite series. Four different hybrid tails were investigated, shown in Table IV. The identified hydrodynamic functions Γ_2 are shown for tail1 and tai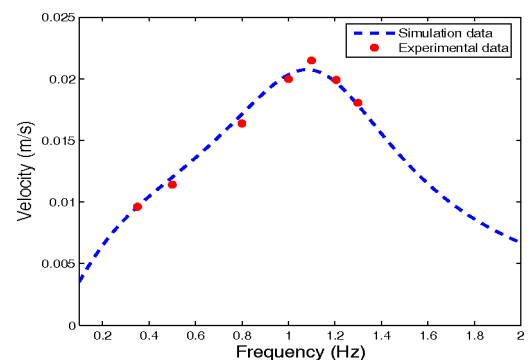l2 in Fig. 11. It can be seen that, while the hydrodynamic functions are qualitatively close to each other, they are shape-dependent. The predicted speeds match the experimental data well, as shown in Fig 12. Intuitively, within the actuation bandwidth of IPMC, the achieved speed increases with the actuation frequency. As the frequency gets relatively high, the bending amplitude of IPMC decreases. Thus, for each tail, there is an optimal frequency under which the fish reaches the highest speed. Both the optimal frequency and the corresponding highest speed depend on the dimensions of both IPMC and passive fin, which can be predicted by the speed model.

V. CONCLUSION AND FUTURE WORK

In this paper, the modeling of steady-state cruising motion was presented for an IPMC-propelled robotic fish. The model incorporates both IPMC actuation dynamics and hydrodynamic interactions, and it further considers the effect of a passive fin on the robot performance. The model was verified in experiments for robotic fish with different tail dimensions. The model will be useful for design and control of the robot to meet the tradeoff between locomotion speed and energy consumption.

Although a focus of the modeling work here is to understand how the steady-state speed of the robot depends on the fin design and actuation input, the approach to modeling IPMC fins in underwater operation holds promise for understanding general motions and maneuvers of the robotic fish. We will extend the presented model to investigate steady turning motion under periodic but asymmetric (left versus right) actuation of the IPMC, as well as unsteady motions such as the acceleration and deceleration of the robot. Path planning and control of the robotic fish will also be examined. In addition, we are exploring the use of IPMC as flow sensors for robotic fish control.

We note that other ionic-type EAPs, in particular, conjugated polymers have also been explored as propelling mechanisms for robotic fish [22]–[24]. The focus of the current paper is on incorporating both IPMC actuation dynamics and hydrodynamics into modeling. The comparison of IPMC-enabled robotic fish with those of conjugated polymer-enabled ones is outside of the scope of this paper, although a clear distinction is that a conjugated polymer fin needs either to be encapsulated or to work in electrolyte for long-term operation [24]. However, the presented approach to coupling actuation and hydrodynamic effects can be potentially extended to conjugated polymer-enabled robotic fish by using corresponding actuation models, e.g., [43].

APPENDIX A

DERIVATION OF $M(L,s)$, $F_c(L,s)$, AND $F_d(z,s)$ IN SECTION III-C

Based on the principle of replacement in Section III-C, one gets, for $0 \leq z \leq L$

$$M_{\text{IPMC}}(z,s) = \int_z^L F_d(\tau)(\tau - z)\,d\tau + F_c(L,s)(L-z) + M(L,s).$$

At $z = L$, one gets

$$M(L,s) = M_{\text{IPMC}}(L,s)$$

which is (23). Then, one takes the derivative with respect to z on both sides of (22) as

$$\frac{\partial M_{\text{IPMC}}(z,s)}{\partial z} = \int_z^L \frac{\partial (F_d(\tau)(\tau - z))}{\partial z}\,d\tau - F_c(L,s)$$

$$= -\int_z^L F_d(\tau)\,d\tau - F_c(L,s). \quad (53)$$

Letting $z = L$ in (53), one obtains

$$F_c(L,s) = -\left.\frac{\partial M_{\text{IPMC}}(z,s)}{\partial z}\right|_{z=L}.$$

Finally, (22) is obtained by taking the derivative with respect to z on both sides of (53).

APPENDIX B

DERIVATION OF $H_{fi}(s)$

With (22), (21), and definitions of a, b, and c in (27) and (28), (24) can be written as

$$f_{1i}(s) = \frac{V(s)}{M_i}\int_0^L (a\cosh(cz) - b\sinh(cz))\,\varphi_i(z)dz$$

$$+ \frac{M(L,s)\varphi_i'(L)}{M_i}. \quad (54)$$

Denote

$$f_{di} = \int_0^L (a\cosh(cz) - b\sinh(cz))\,\varphi_i(z)dz. \quad (55)$$

Then, (54) can be written as

$$f_i(s) = \frac{V(s)}{M_i}f_{di} + \frac{M(L,s)\varphi_i'(L)}{M_i}. \quad (56)$$

With definition of $\varphi_i(z)$ in (15), (55) can be written as

$$f_{di} = \int_0^L \begin{pmatrix} a(\cosh(cz)\cosh(\lambda_i z) - \cosh(cz)\cos(\lambda_i z)) \\ -\beta_i a(\cosh(cz)\sinh(\lambda_i z) - \cosh(cz)\sin(\lambda_i z)) \\ -b(\sinh(cz)\cosh(\lambda_i z) - \sinh(cz)\cos(\lambda_i z)) \\ +\beta_i b(\sinh(cz)\sinh(\lambda_i z) - \sinh(cz)\sin(\lambda_i z)) \end{pmatrix} dz$$

$$= \int_0^L \begin{pmatrix} a\begin{pmatrix}\cosh(cz+\lambda_i z) + \cosh(cz-\lambda_i z) \\ -\cosh(cz+j\lambda_i z) - \cosh(cz-j\lambda_i z)\end{pmatrix} \\ -\beta_i a\begin{pmatrix}\sinh(cz+\lambda_i z) - \sinh(cz-\lambda_i z) \\ +j\sinh(cz+j\lambda_i z) - j\sinh(cz-j\lambda_i z)\end{pmatrix} \\ -b\begin{pmatrix}\sinh(cz+\lambda_i z) + \sinh(cz-\lambda_i z) \\ -\sinh(cz+j\lambda_i z) - \sinh(cz-j\lambda_i z)\end{pmatrix} \\ +\beta_i b\begin{pmatrix}\cosh(cz+\lambda_i z) - \cosh(cz-\lambda_i z) \\ +j\cosh(cz+j\lambda_i z) - j\cosh(cz-j\lambda_i z)\end{pmatrix} \end{pmatrix} dz. $$

$$(57)$$

After integrating (57), we obtain

$$f_{di} = (a-b)(a_L + b_L - c_L - d_L)$$

$$- \beta_i(a-b)(a_L - b_L + jc_L - jd_L) \quad (58)$$

where a_L, b_L, c_L, and d_L are defined in (29) and (30). With (23) and (58), (56) can be written as

$$
\begin{aligned}
f_{1i}(s) &= \frac{V(s)}{2M_i} \begin{pmatrix} (a-b)(a_L + b_L - c_L - d_L) \\ -\beta_i(a-b)(a_L - b_L + jc_L - jd_L) \end{pmatrix} \\
&+ \frac{\alpha_0 W K k_e (\gamma(s) - \tanh(\gamma(s)))}{(s\gamma(s) + K \tanh(\gamma(s)))} \frac{\varphi_i'(L)V(s)}{(1 + r_2\theta(s))\cosh(cL)}.
\end{aligned}
\tag{59}
$$

Then, one can obtain the transfer functions (26) from (59).

APPENDIX C

DERIVATION OF ACTUATION MODEL FOR HYBRID TAIL

With (24), (39) can be written as

$$
f_{2i}(s) = f_{1i}(s) + \frac{F_{\text{tail}}(s)\varphi_i(L_0) + M_{\text{tail}}(s)\varphi_i'(L_0)}{M_i}.
\tag{60}
$$

With (25) and (37), (60) can be written as

$$
\begin{aligned}
f_{2i} &= H_{fi}(s)V(s) \\
&- \frac{M_s}{M_i} \begin{bmatrix} [\varphi_i'(L_0)k_a + \varphi_i(L_0)k_b] w'(L_0, s) \\ + [\varphi_i'(L_0)k_b + \varphi_i'(L_0)k_c] w(L_0, s) \end{bmatrix}.
\end{aligned}
\tag{61}
$$

The general coordinate $q_{2i}(s)$ is

$$
q_{2i}(s) = Q_i(s)f_{2i}(s).
\tag{62}
$$

Then, with (61) and (62), (14) can be written as x

$$
\begin{aligned}
w(z, s) &= \sum_{i=1}^{\infty} \varphi_i(L_0) Q_i(s) H_{fi}(s) V(s) \\
&- \sum_{i=1}^{\infty} \frac{M_s \varphi_i(L_0) Q_i(s)}{M_i} \\
&\times \begin{bmatrix} [\varphi_i'(L_0)k_a + \varphi_i(L_0)k_b] w'(L_0, s) \\ + [\varphi_i'(L_0)k_b + \varphi_i(L_0)k_c] w(L_0, s) \end{bmatrix}.
\end{aligned}
\tag{63}
$$

From (31), (63) can be written as

$$
\begin{aligned}
w(z, s) &= H_1(s)V(s) - \sum_{i=1}^{\infty} \frac{M_s \varphi_i(L_0) Q_i(s)}{M_i} \\
&\times \begin{bmatrix} [\varphi_i'(L_0)k_a + \varphi_i(L_0)k_b] w'(L_0, s) \\ + [\varphi_i'(L_0)k_b + \varphi_i(L_0)k_c] w(L_0, s) \end{bmatrix}
\end{aligned}
\tag{64}
$$

and with (32), the slope can be written as

$$
\begin{aligned}
w'(z, s) &= H_{1d}(s)V(s) - \sum_{i=1}^{\infty} \frac{M_s \varphi_i'(L_0) Q_i(s)}{M_i} \\
&\times \begin{bmatrix} [\varphi_i'(L_0)k_a + \varphi_i(L_0)k_b] w'(L_0, s) \\ + [\varphi_i'(L_0)k_b + \varphi_i(L_0)k_c] w(L_0, s) \end{bmatrix}.
\end{aligned}
\tag{65}
$$

With the definition of A_s, E_s, B_s, C_s, F_s, and J_s in (42)–(46), one can write (64) and (65) as

$$
w(L_0, s) = A_s V(s) - B_s w'(L_0, s) - C_s w(L_0, s)
\tag{66}
$$

$$
w'(L_0, s) = E_s V(s) - F_s w'(L_0, s) - J_s w(L_0, s).
\tag{67}
$$

Solving (66) and (67) for $w(L_0, s)$ and $w'(L_0, s)$ gives

$$
w(L_0, s) = \frac{(1 + F_s)A_s - B_s E_s}{(1 + C_s)(1 + F_s) - B_s J_s} V(s)
$$

$$
w'(L_0, s) = \frac{(1 + C_s)E_s - A_s J_s}{(1 + C_s)(1 + F_s) - B_s J_s} V(s).
$$

Then, one can obtain the transfer functions (40) and (41).

REFERENCES

[1] G. V. Lauder and E. G. Drucker, "Morphology and experimental hydrodynamics of fish fin control surfaces," *IEEE J. Ocean. Eng.*, vol. 29, no. 3, pp. 556–571, Jul. 2004.

[2] F. E. Fish and G. V. Lauder, "Passive and active flow control by swimming fishes and mammals," *Annu. Rev. Fluid Mech.*, vol. 38, pp. 193–224, 2006.

[3] M. J. Lighthill, "Large-amplitude elongated-body theory of fish locomotion," in *Proc. R. Soc. Lond. B*, 1971, vol. 179, pp. 125–138.

[4] T. Y. Wu, "Mathematical biofluid dynamics and mechanophysiology of fish locomotion," *Math. Methods Appl. Sci.*, vol. 24, pp. 1541–1564, 2001.

[5] U. K. Muller, E. J. Stamhuis, and J. J. Videler, "Riding the waves: The role of the body wave in undulatory fish swimming," *Integr. Comp. Biol.*, vol. 42, pp. 981–987, 2002.

[6] J. Peng, J. O. Dabiri, P. G. Madden, and G. V. Lauder, "Non-invasive measurement of instantaneous forces during aquatic locomotion: A case study of the bluegill sunfish pectoral fin," *J. Exp. Biol.*, vol. 210, pp. 685–698, 2007.

[7] R. Mittal, "Computational modeling in biohydrodynamics: Trends, challenges, and recent advances," *IEEE J. Ocean. Eng.*, vol. 29, no. 3, pp. 595–604, Jul. 2004.

[8] M. S. Triantafyllou and G. S. Triantafyllou, "An efficient swimming machine," *Sci. Amer.*, vol. 272, pp. 64–71, 1995.

[9] S. Guo, T. Fukuda, and K. Asaka, "A new type of fish-like underwater microrobot," *IEEE/ASME Trans. Mechatronics*, vol. 8, no. 1, pp. 136–141, Mar. 2003.

[10] H. Hu, J. Liu, I. Dukes, and G. Francis, "Design of 3D swim patterns for autonomous robotic fish," in *Proc. 2006 IEEE/RSJ Int. Conf. Intell. Robots Syst.*, Beijing, China, 2006, pp. 2406–2411.

[11] B. Kim, D. Kim, J. Jung, and J. Park, "A biomimetic undulatory tadpole robot using ionic polymer–metal composite actuators," *Smart Mater. Struct.*, vol. 14, pp. 1579–1585, 2005.

[12] X. Tan, D. Kim, N. Usher, D. Laboy, J.Jackson, A.Kapetanovic, J. Rapai, B. Sabadus, and X. Zhou, "An autonomous robotic fish for mobile sensing," in *Proc. IEEE/RSJ Int. Conf. Intell. Robots Syst.*, Beijing, China, 2006, pp. 5424–5429.

[13] K. A. Morgansen, B. I. Triplett, and D. J. Klein, "Geometric methods for modeling and control of free-swimming fin-actuated underwater vehicles," *IEEE Trans. Robot.*, vol. 23, no. 6, pp. 1184–1199, Dec. 2007.

[14] P. V. Alvarado and K. Youcef-Toumi, "Design of machines with compliant bodies for biomimetic locomotion in liquid environments," *Trans. ASME, J. Dyn. Syst., Meas. Control*, vol. 128, pp. 3–13, 2006.

[15] G. V. Lauder, E. J. Anderson, J. Tangorra, and P. G. A. Madden, "Fish biorobotics: Kinematics and hydrodynamics of self-propulsion," *J. Exp. Biol.*, vol. 210, pp. 2767–2780, 2007.

[16] M. S. Triantafyllou, D. K. P. Yue, and G. S. Triantafyllou, "Hydrodynamics of fishlike swimming," *Annu. Rev. Fluid Mech.*, vol. 32, pp. 33–53, 2000.

[17] P. R. Bandyopadhyay, "Maneuvering hydrodynamics of fish and small underwater vehicles," *Integr. Comparative Biol.*, vol. 42, pp. 102–117, 2002.

[18] M. Epstein, J. E. Colgate, and M. A. MacIver, "Generating thrust with a biologically-inspired robotic ribbon fin," in *Proc. 2006 IEEE/RSJ Int. Conf. Intell. Robots Syst.*, Beijing, China, pp. 2412–2417.

[19] J. W. Paquette and K. J. Kim, "Ionomeric electroactive polymer artificial muscle for naval applications," *IEEE J. Ocean. Eng.*, vol. 29, no. 3, pp. 729–738, Jul. 2004.

[20] J. D. W. Madden, B. Schmid, M. Hechinger, S. R. Lafontaine, P. G. A. Madden, F. S. Hover, R. Kimball, and I. W. Hunter, "Application of polypyrrole actuators: Feasibility of variable camber foils," *IEEE J. Ocean. Eng.*, vol. 29, no. 3, pp. 738–749, Jul. 2004.

[21] M. Shahinpoor and K. Kim, "Ionic polymer–metal composites: I. Fundamentals," *Smart Mater. Struct.*, vol. 10, pp. 819–833, 2001.

[22] J. Tangorra, P. Anquetil, T. Fofonoff, A. Chen, M. D. Zio, and I. Hunter, "The application of conducting polymers to a biorobotic fin propulsor," *Bioinspiration Biomimetics*, vol. 2, pp. S6–S17, 2007.

[23] G. Alici, G. Spinks, N. N. Huynh, L. Sarmadi, and R. Minato, "Establishment of a biomimetic device based on tri-layer polymer actuators łpropulsion fins," *Bioinspiration Biomimetics*, vol. 2, pp. S18–S30, 2007.

[24] S. McGovern, G. Alici, V. T. Truong, and G. Spinks, "Finding NEMO (Novel Electromaterial Muscle Oscillator): A polypyrrole powered robotic fish with real-time wireless speed and directional control," *Smart Mater. Struct.*, vol. 18, pp. 095 009-1–095 009-10, 2009.

[25] M. Anton, A. Punning, A. Aabloo, M. Listak, and M. Kruusmaa, "Towards a biomimetic EAP robot," in *Proc. Towards Auton. Mobile Robots*, 2004, pp. 1–7.

[26] E. Mbemmo, Z. Chen, S. Shatara, and X. Tan, "Modeling of biomimetic robotic fish propelled by an ionic polymer–metal composite actuator," in *Proc. IEEE Int. Conf. Robot. Autom.*, 2008, pp. 689–694.

[27] N. Kamamichi, M. Yamakita, K. Asaka, and Z.-W. Luo, "A snake-like swimming robot using IPMC actuator//sensor," in *Proc. IEEE Conf. Robot. Autom.*, Orlando, FL, 2006, pp. 1812–1817.

[28] K. J. Kim and M. Shahinpoor, "Ionic polymer–metal composites: II. Manufacturing techniques," *Smart Mater. Struct.*, vol. 12, pp. 65–79, 2003.

[29] J. Yu, L. Wang, and M. Tan, "Geometric optimization of relative link lengths for biomimetic robotic fish," *IEEE Trans. Robot.*, vol. 23, no. 2, pp. 382–386, Apr. 2007.

[30] S. Zhao and J. Yuh, "Experimental study on advanced underwater robot control," *IEEE Trans. Robot.*, vol. 21, no. 4, pp. 695–703, Aug. 2005.

[31] F. Boyer, M. Porez, and W. Khalil, "Macro-continuous computed torque algorithm for a three-dimensional eel-like robot," *IEEE Trans. Robot.*, vol. 22, no. 4, pp. 763–775, Aug. 2006.

[32] W. Yim, J. Lee, and K. J. Kim, "An artificial muscle actuator for biomimetic underwater propulsors," *Bioinspiration Biomimetics*, vol. 2, pp. S31–S41, 2007.

[33] P. Brunetto, L. Fortuna, S. Graziani, and S. Strazzeri, "A model of ionic polymer–metal composite actuators in underwater operations," *Smart Mater. Struct.*, vol. 17, no. 2, pp. 025 029-1–025 029-12, 2008.

[34] K. Abdelnour, E. Mancia, S. D. Peterson, and M. Porfiri, "Hydrodynamics of underwater propulsors based on ionic polymer metal composites: A numerical study," *Smart Mater. Struct.*, vol. 18, no. 8, pp. 085 006-1–085 006-11, 2009.

[35] S. D. Peterson, M. Porfiri, and A. Rovardi, "A particle image velocimetry study of vibrating ionic polymer metal composites in aqueous environments," *IEEE/ASME Trans. Mechatronics*, vol. 14, no. 4, pp. 474–483, Aug. 2009.

[36] M. J. Lighthill, "Note on the swimming of slender fish," *J. Fluid Mech.*, vol. 9, pp. 305–317, 1960.

[37] M. J. Lighthill, "Aquatic animal propulsion of high hydromechanical efficiency," *J. Fluid Mech.*, vol. 44, pp. 265–301, 1970.

[38] Z. Chen and X. Tan, "A control-oriented and physics-based model for ionic polymer-metal composite actuators," *IEEE/ASME Trans. Mechatronics*, vol. 13, no. 5, pp. 519–529, Oct. 2008.

[39] R. W. Clough and J. Penzien, *Dynamics of Structures*. New York: McGraw-Hill, 1993.

[40] J. E. Sader, "Frequency response of cantilever beams immersed in viscous fluids with applications to the atomic force microscope," *J. Appl. Phys.*, vol. 84, no. 1, pp. 64–76, 1998.

[41] P. Lu and K. Lee, "An alternative derivation of dynamic admittance matrix of piezoelectric cantilever bimorph," *J. Sound Vib.*, vol. 266, pp. 723–735, 2003.

[42] S. Nemat-Nasser and J. Li, "Electromechanical response of ionic polymer–metal composites," *J. Appl. Phys.*, vol. 87, no. 7, pp. 3321–3331, 2000.

[43] Y. Fang, X. Tan, Y. Shen, N. Xi, and G. Alici, "A scalable model for trilayer conjugated polymer actuators and its experimental validation," *Mater. Sci. Eng. C*, vol. 28, no. 3, pp. 421–428, 2008.

Zheng Chen (S'05) received the B.S. degree in electrical engineering and the M.S. degree in control science and engineering from Zhejiang University, Hangzhou, China, in 1999 and 2002, respectively. He is currently working toward the Ph.D. degree in electrical and computer engineering at Michigan State University (MSU), East Lansing.

His current research interests include fabrication, modeling and control of electrical-active polymers (EAPs), biomimetic robots, EAP-based smart microsystems, and optimal control using neural networks.

Mr. Chen was the recipient of the Summer Dissertation Fellowship in 2005 and the Dissertation Completion Fellowship in 2009, both from MSU Graduate School. He also received an Honorable Mention for the Fitch Beach Outstanding Graduate Research Award from MSU College of Engineering in 2008.

Stephan Shatara received the B.S. and M.S. degrees in electrical and computer engineering from Michigan State University, East Lansing, in 2006 and 2008, respectively.

He was engaged in the development of small biomimetic robotic fish with onboard acoustic-based ranging. He is currently a Senior Systems Engineer with Motorola, Inc., Schaumburg, IL, where he is involved in the design of two-way radio infrastructure for the government and public safety sectors.
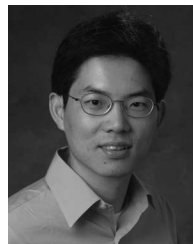
Xiaobo Tan (S'97–M'02) received the Bachelor's and Master's degrees in automatic control from Tsinghua University, Beijing, China, in 1995 and 1998, respectively, and the Ph.D. degree in electrical and computer engineering from the University of Maryland, College Park, in 2002.

From September 2002 to July 2004, he was a Research Associate with the Institute for Systems Research, University of Maryland. Since August 2004, he has been an Assistant Professor in the Department of Electrical and Computer Engineering, Michigan State University, East Lansing, where he is also the Director of the Smart Microsystems Laboratory. His current research interests include electroactive polymer sensors and actuators, biomimetic robotic fish, mobile sensing in aquatic environments, modeling and control of smart materials, and collaborative control of autonomous systems. He is an Associate Editor of *Automatica*.

Dr. Tan is a member of the IEEE Control Systems Society Conference Editorial Board. He was a Guest Editor of the *IEEE Control Systems Magazine* for its February 2009 issue's special section on modeling and control of hysteresis. He received a National Science Foundation CAREER Award in 2006.